

The X-ray Halo of GX 13+1

Randall K. Smith, Richard J. Edgar

Smithsonian Astrophysical Observatory, 60 Garden St., Cambridge, MA 02138

rsmith,redgar@cfa.harvard.edu

and

Richard A. Shafer

Code 685, Laboratory for Astronomy and Space Physics, NASA Goddard Space Flight Center, Greenbelt, MD 20771

richard.shafer@gsfc.nasa.gov

ABSTRACT

We present observations of the X-ray halo around the LMXB GX 13+1 from the *Chandra* X-ray telescope. The halo is caused by scattering in interstellar dust grains, and we use it to diagnose the line-of-sight position, size distribution, and density of the grains. Using the intrinsic energy resolution of *Chandra*'s ACIS CCDs and the recent calibration observation of the *Chandra* point spread function (PSF), we were able to extract the halo fraction as a function of energy and off-axis angle. We define a new quantity, the “halo coefficient,” or the total halo intensity relative to the source at 1 keV, and measure it to be $1.5^{+0.5}_{-0.1}$ for GX 13+1. We find a relationship between this value and the dust size, density, and hydrogen column density along the line of sight to GX 13+1. We also conclude that our data does not agree with “fluffy” dust models that earlier X-ray halo observations have supported, and that models including an additional large dust grain population are not supported by these data.

Subject headings: dust — scattering — X-rays: binaries — X-rays: ISM

1. Introduction

X-ray halos are created by the small-angle scattering of X-rays passing through dust grains in the interstellar medium. The spectral and spatial characteristics of X-ray halos are

determined by the size, line of sight distribution, and composition of dust grains, with a bias towards larger dust grains which are the primary sites for X-ray scattering. These larger grains hold much of the mass that is in dust grains and they are difficult to detect in other wavebands. In this paper, we will describe how observations of the halo around GX 13+1 can be used to place limits on dust grain models, specifically on the population of larger grains.

GX 13+1, a low-mass X-ray binary (LMXB), is a bright highly-absorbed X-ray source. IR spectral observations by Bandyopadhyay *et al.* (1999) show that the secondary star is likely a K5 giant, and they calculate a distance of 7 ± 1 kpc for the system. GX 13+1 has been classified as an atoll source (Hasinger & van der Klis 1989), although it belongs to the small subclass of atoll sources that are persistently bright. The X-ray halo around GX 13+1 was first described by Catura (1983), who used *Einstein* HRI data and measured a total halo flux equal to 0.18 ± 0.02 of the source flux in the HRI band (0.1-6 keV). However, Catura noted that systematic uncertainties in the observation probably lead to an underestimate of the halo strength. Subsequently, Mauche & Gorenstein (1986) used *Einstein* IPC observations of GX 13+1 to measure a halo fraction of 0.17 ± 0.01 in the IPC band (0.1-6.4 keV). In 1995, Predehl & Schmitt measured the X-ray halo of GX 13+1 using only 47 seconds of observations from the ROSAT All-Sky Survey. They found a much brighter X-ray halo, 0.37 ± 0.04 of the source flux in the PSPC band (0.08-2.9 keV). The discrepancy between the *Einstein* and *ROSAT* observations has not been discussed, but we will show it is due to the different energy bands of the instruments.

Measurements of X-ray halos have been used to place limits on the dust grain density (Mathis *et al.* 1995), as well as the dust size distribution (Witt, Smith & Dwek 2001). The *Chandra* observations provide the far higher angular and energy resolution than has been available, so we can extract the halo fraction as a function of off-axis angle and energy. By comparing the observed halo fraction to a selection of dust models, we put limits on the density of the dust and the relative population of large grains.

2. Theoretical Background

The theory of X-ray halos was first discussed in an astrophysical context by Overbeck (1965), and has since been refined by a number of authors (Mauche & Gorenstein 1986; Mathis & Lee 1991; Smith & Dwek 1998). We briefly review the theory here.

The fundamental quantity is the differential scattering cross section $d\sigma/d\Omega$, which can be calculated using either the exact Mie solution or the Rayleigh-Gans (RG) approximation;

see Smith & Dwek (1998) for a discussion. The RG approximation is derived by assuming each volume dV in the dust scatters X-rays via Rayleigh scattering, and then integrating the result over the grain volume. Analytically, this gives

$$\frac{d\sigma(\theta_{\text{sca}})}{d\Omega} = 1.1 \text{ cm}^2 \text{sr}^{-1} \left(\frac{2Z}{M} \right)^2 \left(\frac{\rho}{3g \text{cm}^{-3}} \right)^2 a_{\mu\text{m}}^6 \left(\frac{F(E)}{Z} \right)^2 \Phi^2(\theta_{\text{sca}}) \quad (1)$$

where a is the grain radius, Z is the mean atomic charge, M the mean atomic weight (in amu), ρ the mass density, E the X-ray energy in keV, $F(E)$ the atomic scattering factor (Henke 1981), θ_{sca} the scattering angle, and $\Phi^2(\theta_{\text{sca}})$ the scattering form factor (Mathis & Lee 1991). For homogeneous spherical grains, the form factor is given by

$$\Phi^2(\theta_{\text{sca}}) = 3(\sin u - u \cos u)/u^3 \quad (2)$$

where $u = 4\pi a \sin(\theta_{\text{sca}}/2)/\lambda \approx 2\pi a \theta_{\text{sca}} E/hc$.

Smith & Dwek (1998) showed that the RG approximation will overestimate the total scattering if the energy of the X-rays (in keV) is not substantially larger than the size of the dust grains (in μm), and suggested 2 keV as a minimum energy for most ISM dust models.

By integrating the scattering cross section over the line of sight geometry, the source spectrum, and the dust size distribution we get (considering single scatterings only) the halo surface brightness at angle θ from the source:

$$I_{\text{sca}}(\theta) = F_X N_H \int dE S(E) \int da n(a) \int_0^1 dx \frac{f(x)}{(1-x)^2} \frac{d\sigma}{d\Omega} \quad (3)$$

where F_X is the total source flux, N_H is the hydrogen column density, $S(E)$ is the (normalized) X-ray spectrum, and $n(a)da$ is the dust grain size distribution. Here $f(x)$ is the density of hydrogen at distance xD from the observer divided by the line of sight average density, where D is the distance to the source (Mathis & Lee 1991).

Of course if the column density is sufficiently large, individual X-rays may be scattered multiple times. Mathis & Lee (1991) showed that for $\tau_{\text{sca}} > 1.3$, multiple scatterings dominate over single scattering, tending to broaden the halo. The scattering cross section depends upon the X-ray energy and the dust model; Table 1 of Mathis & Lee (1991) shows that $\sigma_{\text{sca}} = 9.03 \times 10^{-23} E_{\text{keV}}^{-2}$ for dust models such as Mathis, Rumpl & Nordsieck (1977; MRN) or Draine & Lee (1984). For $N_H \approx 2.9 \times 10^{22} \text{ cm}^{-2}$ (see §3.1), this corresponds to $\tau_{\text{sca}} = 2.6 E_{\text{keV}}^{-2}$. Above 2 keV, therefore, multiple scattering should not be a significant effect. Below 2 keV, we can expect that the RG approximation will somewhat overestimate the total halo intensity and the single scattering approximation will underestimate the radial extent of the halo.

3. Observations and Analysis

GX 13+1 was observed with the *Chandra* ACIS-I array (chips I0-3, S2, S3) for 9.74 ksec on August 7th, 2000. GX 13+1 was at the aimpoint, and as can be seen in Figure 1, a bright halo was observed although as expected the source itself suffered from severe pile-up. We processed the data using the *Chandra* data system software version R4CU5UPD14.1, and used CIAO version 2.2 for our analysis.

The ACIS-I CCDs were damaged early in the *Chandra* mission by low-energy protons. As a result the energy resolution decreased; at 1.5 keV, the FWHM on ACIS-I3 now varies from ~ 100 eV to ~ 150 eV, depending on the distance from the CCD readout. Based on this resolution and the quantity of data, we decided to bin the data into 100 eV and 200 eV bins (for energies less than and greater than 2 keV, respectively).

3.1. Spectral Analysis

The X-ray halo is directly proportional to the source spectrum, so any uncertainties in the spectral analysis will be reflected in the halo analysis. Ideally, the spectral measurement would be high-resolution and contemporaneous; for this observation, however, we have only the ACIS-I data, which are heavily affected by pileup. In CCD detectors such as the ACIS-I, pileup occurs when two or more photons impact the same or adjacent pixels within a single 3.2 second frame. This can mimic a single photon with energy equal to the sum of the photon energies, or it can change the event “grade” from a good X-ray detection (grades 0, 2, 3, 4, or 6) to a rejected likely cosmic-ray event (grade 7) (*Chandra Proposers’ Observatory Guide*, Rev. 4.0, p 106). In GX 13+1, the core pileup was large enough that all photons within a 3'' of the source migrated to grade 7 and were automatically rejected; nearby regions somewhat further off-axis were also contaminated by pile-up.

Despite this, the source spectrum can be extracted from the “transfer streak,” which appears as a line connecting the detector aimpoint and the chip readout in Figure 1. During the 42 ms frame transfer of the ACIS CCDs, X-rays from the source continue to arrive at the aimpoint and are as a result “mis-positioned” along the axis of the transfer by the *Chandra* processing software. In 9.74 ksec of observing, the ACIS spends ~ 128 seconds in frame transfer mode. We extracted $\sim 31,000$ events in an 11×908 pixel strip around this streak (avoiding the near-aimpoint region which will be affected to a lesser degree by pileup). We were also concerned about pileup in the transfer streak. However, the streak has only 10.3 ± 3.2 counts per 3.2 second CCD frame spread over a 11×908 pixel region, so pileup there is not significant.

The in-flight spectral response of the ACIS-I detectors during frame transfer is not yet specifically calibrated. We assumed all the events in the transfer streak originated on-axis with the normal effective area in calculating the detector response, but there is a known effect that slightly reduces the quantum efficiency of the CCDs for photons above 3-4 keV (M. Bautz 2002 private communication). We also found that the ratio of grade 0 (single-pixel) events to all good events (grades 0,2,3,4, and 6) in the transfer streak was significantly lower than elsewhere on the ACIS-I chips. This may or may not affect the spectrum; the ACIS calibration team is working on the problem.

Other non-contemporaneous X-ray observations of GX 13+1 exist. GX 13+1 is regularly observed by the RXTE All-sky Monitor (ASM), although unfortunately it was not observed for a period of ~ 10 days surrounding the Chandra observation. The long-term ASM lightcurve shows that the luminosity in the 1.3-12.1 keV bandpass is relatively constant, with intrinsic variations of $\sim 50\%$ (Homan *et al.* 1998). GX 13+1 was also observed by ASCA for 18.8 ksec in September 1994. We extracted the GIS data, which have nearly 10^6 counts; the source was blocked out in the SIS detectors. The flux observed by ASCA in the 1-10 keV band is $\sim 25\%$ larger than was observed by *Chandra*, likely due to fluctuations in the source itself.

The observed halo intensity at energy E is proportional to the observed source flux at energy E and the column density of dust along the line of sight. To estimate these we fit a range of spectral models and examined the results. Intrinsically, the X-ray spectra of LMXBs vary widely due to the many possible viewing angles and emission mechanisms. We therefore considered a number of different models, following the Christian & Swank (1997) analysis of the X-ray emission for a sample of LMXBs. We used blackbody (BB), power law (PL), and thermal bremsstrahlung (TB) models, along with a disk blackbody (DBB; see Mitsuda *et al.* 1984, Makishima *et al.* 1986) model. In addition, we fit the spectrum using a series of top-hat functions, roughly matching the ACIS-I resolution by using 100 eV spacing from 1-2 keV and 200 eV spacing from 2-4 keV. This approach measures the observed flux (with errors) in each 100 or 200 eV band without reference to any specific model.

All of these models led to a formally acceptable value of χ^2 , due to the low count rate and energy resolution in the transfer streak data. We calculated the X-ray flux as a function of energy for each of these models, as shown in Figure 2. The summed top-hat model results in similar fluxes as the different spectral models, and the errors on the top-hat amplitudes are on the same scale as the variations in the spectral models. We will use the top-hat fluxes and errors for the following analysis.

The best-fit column density for these models varied from 1.99 to 4.17×10^{22} cm $^{-2}$ depending on the source model used. Given the issues with the transfer streak detector response,

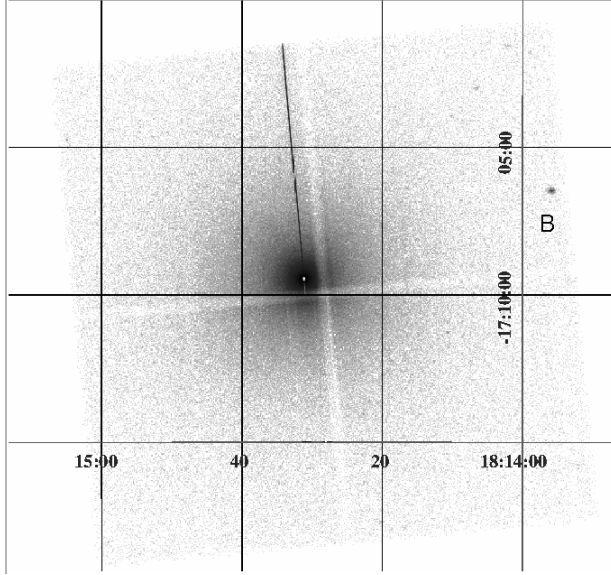


Fig. 1.— *Chandra* ACIS-I image of GX 13+1. The transfer streak can be seen extending from the central source, and the serendipitous source “B” is marked. Also notable are the chip gaps of the ACIS-I array.

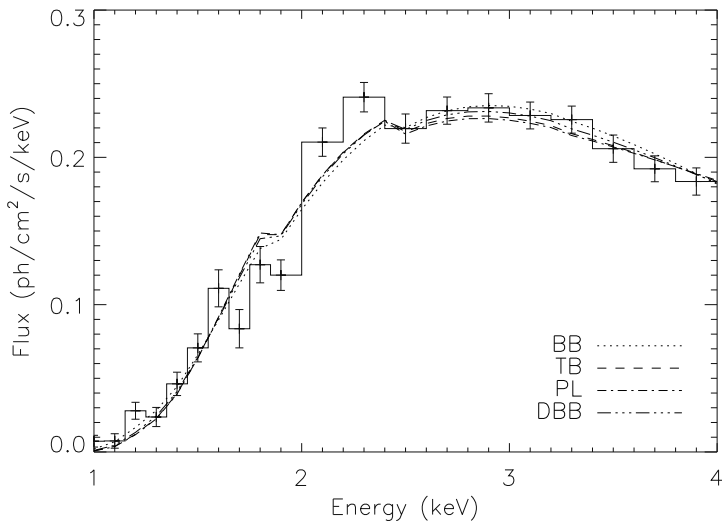


Fig. 2.— Best-fit X-ray flux from GX 13+1 after fitting the observed spectrum with blackbody (BB), power law (PL), thermal bremsstrahlung (TB), and a disk blackbody (DBB) model. The histogram shows the fluxes and errors found using a model consisting of a sum of top-hat functions. Note that despite the wide range of models, the flux in each energy band varies only slightly.

we decided not to use these N_{H} results. The absorption column density has been measured with other X-ray satellites; Ueda *et al.* (2001) found $N_{\text{H}} = 2.9 \pm 0.1 \times 10^{22} \text{ cm}^{-2}$ from ASCA GIS and SIS observations (with $> 10^6$ counts), which agrees with the value found by Schulz, Hasinger & Trümper (1989) from EXOSAT ME data. Garcia *et al.* (1992) placed an upper limit of $A_V \lesssim 14.4$ based on measurements in the J, H, and K bands and assuming the spectrum rose no faster than the Jeans tail of a blackbody. Using the conversion from $N_{\text{H}}/A_V = 1.9 \times 10^{21} \text{ cm}^{-2}/\text{mag}$ (Seward 2000), this is equivalent to $N_{\text{H}} \lesssim 2.7 \times 10^{22} \text{ cm}^{-2}$.

3.2. Imaging Analysis

Measuring the radial profile of GX 13+1 is a multi-step process. We began by removing any serendipitous sources from the image. We then selected an energy and a radial grid, based on the instrumental response and the quantity of data available. We filtered the data using the CCD energy measurement, and extracted the counts in the radial profile using concentric annuli centered on the source. Then we made exposure maps for each energy band. After filtering out the regions with serendipitous sources, we extracted the effective “radial exposure” using the same concentric annuli, for each energy band. Dividing the radial profile of the counts in each band by the effective area and exposure time gave us the corrected radial profile in units of photons $\text{cm}^{-2} \text{ s}^{-1} \text{ arcmin}^{-2}$ per energy band. We then divided this by the observed source flux in each band to get the fractional radial profile in units of source fraction arcmin^{-2} . This result is really the X-ray halo convolved with the *Chandra* PSF, plus the PSF from the source itself. However, the *Chandra* PSF is small enough that we will neglect any scattering of the X-ray halo by the telescope.

We searched for sources in the field of view using the CIAO tool *celldetect*. Since removing a false source merely reduces the signal to noise slightly, while including a source mistakenly would add a systematic error, we decided to accept any source found with significance greater than 4σ . This resulted in six sources, listed in Table 1. A search using *Simbad* showed no known sources with $10''$ of these positions. The *Simbad* search found 39 objects in the field of view, including stars, IRAS objects, and a supernova remnant (G13.5+0.2). None of these sources could be detected in the data, although we note source D is inside the remnant.

The X-ray halo of GX 13+1 fills the ACIS-I field of view, as can be seen in Figure 1. However, the central $3''$ region around the source has no data due to severe pileup, so the source position must be inferred. We estimated the source position by assuming it was on the line defined by the transfer streak and centering using the contours of the data. We found the position of GX 13+1 to be RA,Dec = 18:14:31.065, -17:09:26.02 (J2000), with an

estimated error of $0.3''$. This is $0.3''$ distant from the position measured by Berendsen *et al.* (2000) using radio observations of GX 13+1 with the ATCA. The halo appears to be radially symmetric about the source, as expected from previous observations. We confirmed this by examining the data in various radial bins as a function of azimuthal angle. The data showed no significant variation as a function of angle. We were therefore justified in extracting the radial profile of the X-ray halo by summing the data in annular rings in our selected energy bands.

Pileup substantially affects the central radial bins, so we had to determine where it drops off. This is difficult to estimate *a priori*, since pileup can occur not only when two X-rays strike the same pixel within a single frame time, but also when the two X-rays hit adjacent pixels. Depending on the details of the interaction of the X-ray in the CCD, pileup may lead to events not being recognized, or being rejected, or being identified with the wrong energy and/or a modified grade. We therefore estimated the pileup rate phenomenologically by examining the radial profiles of different grade events. When the count rate is low, the ratio of event grades should tend to a constant which depends on the spectrum. In Figure 3(a) we plot the radial profile of good (grade 0,2,3,4, and 6) events, along with the profile of just grade 0 (single-pixel), and grade 6 (four-pixel) events. Figure 3(b) shows the ratio of grade 0 and grade 6 events to the total as a function of radius, along with the limiting ratio found far from the source. This is not a perfect estimate of the ratio close to the source since the X-ray halo will have some spectral differences from the source, but we do not expect the difference to be substantial. As Figure 3(b) shows, pileup/grade migration is a noticeable effect as far as $50''$ from the source. We can derive a similar result analytically as well. According to the *Chandra* proposers' guide, a pileup fraction of 10% will impact the resulting image or spectrum. Using the 3.2 second ACIS frame time and a poisson-distributed count rate, 10% pileup (or two photons in a single 3×3 pixel grid in one frame) corresponds to a rate of $0.0037 \text{ cts s}^{-1} \text{ pixel}^{-1}$. As Figure 3 shows, this is the rate found within $\sim 20''$ of the source, where the effect of pileup is most severe. To avoid contamination by pileup, we limited our

Table 1: Serendipitous Source List

Source	RA (J2000)	Dec (J2000)	Net Flux (cts/ksec)
B	18:13:55.833	-17:06:28.09	76.8958
C	18:14:37.346	-17:10:39.70	4.77356
D	18:14:10.560	-17:11:17.01	2.17923
E	18:15:04.775	-17:04:46.79	3.00942
F	18:14:02.059	-17:01:33.98	4.25470
G	18:14:06.447	-17:03:00.61	7.05657

halo fits to angles beyond 50''.

Before extracting the radial profile of GX 13+1, we had to select the energy and radial binning. To limit complications due to multiple scattering and problems with the RG approximation, we decided to use only the X-rays above 2 keV. We divided the dataset into 10 energy bands, spaced every 0.2 keV from 2.0-4.0 keV in order to match the ACIS-I resolution. To effectively use *Chandra*'s angular resolution while also roughly equalizing the number of counts in each annulus, we used 99 log-spaced annuli from 10'' to 600'' (plus one from 0-10''). After extracting the radial profiles of the data, we calculated the exposure maps for each energy band and used the same annuli to extract the total effective area at each energy and radius. The serendipitous sources were removed both from the data and the exposure maps, so the results are self-consistent. We then divided the radial profile of event data by that of the exposure map to get a result in physical units of photons cm⁻² s⁻¹ arcmin⁻². This approach does not take into account the varying response of the CCDs. On-axis at 1.5 (4.5) keV, the FWHM is ~ 160 (~ 300) eV, while at the chip readouts, it is ~ 80 (~ 130) eV. Due to the physical layout of the ACIS-I CCDs, small off-axis angles are all far from the chip readouts, while large off-axis angles will contain points both near and far from the chip readouts (Chandra Proposers' Observatory Guide, Rev. 4.0, pp. 74, 86). As a result, there will be a systematic effect in the “average” ACIS response as a function of off-axis angle. Using energies between 2-4 keV summed in broad 200 eV bands will minimize these effects.

The final stage of the analysis is to remove the *Chandra* PSF, which was extremely complicated. The CIAO tool *mkpsf* only models the core of the PSF and is not useful here since we are interested in the PSF 1' or more from the source. With the help of the CXC calibration team, we ran the *Chandra* raytrace model “SAOsac,” (release as of 9/18/01) at a number of energies. SAOsac matches the observed core of the PSF well, but underestimates the wings of the PSF (T. Gaetz, 2002, private communication). The exact amount of the disagreement depends on the X-ray energy and the angle from the source; 500'' from the source it varies from a factor of 2 at 1.5 keV to a factor of 6 at 4.5 keV, comparing the pre-flight calibration data to the model¹.

Unfortunately, the systematic underestimate of the scattering power beyond 50'' led to serious problems in interpretation. To address this, the *Chandra* calibration team observed the bright, lightly-absorbed X-ray binary Her X-1 for 50 ksec on July 1, 2002. Her X-1 is lightly reddened, with $E(B - V) = 0.05$ magnitudes (Liu, van Paradijs, & van den Heuvel 2001), which corresponds to a column density $N_{\text{H}} \approx 3 \times 10^{20} \text{ cm}^{-2}$, although some of this may be internal. The total Galactic column density in the direction of Her X-1 is N_{H}

¹Chapter 15 of the XRCF report, <http://hea-www.harvard.edu/MST/simul/xrcf/report/index.html>

$= 1.8 \times 10^{20} \text{ cm}^{-2}$ (Dickey & Lockman 1990). As a result, the dust-scattered halo is more than $100\times$ weaker than in GX 13+1, and the telescope PSF dominates the radial profile. This Her X-1 image, which clearly shows vignetting from the mirror support structures, confirms this; in GX 13+1, these features are blurred by the X-ray halo.

The Her X-1 data are being analyzed in detail by the CXC calibration team. We did a preliminary analysis using the same procedure as used for the GX 13+1 data, extracting the spectrum from the transfer streak and fitting the flux in 100 eV and 200 eV bands. The observation was done with Her X-1 on ACIS-S3 (a back-illuminated (BI) chip), along with the front-illuminated (FI) I2, I3, and S2 chips. We extracted the radial profile for the BI and FI chips separately, and compared them to each other and to the SAOsac PSFs. The FI and BI profiles agreed with each other at all off-axis angle, and with the SAOsac values for off-axis angles less than $50''$ (see Figure 4). As expected however, beyond $50''$ off-axis, the SAOsac PSF underestimated the data by factors of 2-10, depending on the angle and the X-ray energy. Background appeared to be negligible since the FI and BI profiles match each other even at large angles, despite the significant differences in the background rates on the two types of chips. We summed the FI and BI datasets to get the best measurement of the PSF at each energy.

4. Results

We have now measured the radial profile, in units of fraction of source flux per square arcminute, for both GX 13+1 and Her X-1. Since the source flux has been factored out, subtracting the Her X-1 profile (the best-available point source) from the GX 13+1 profile gives the halo’s surface brightness relative to the source flux as a function of energy and off-axis angle, or the “halo fraction” $H_f(E, \theta)$. We can then calculate the total observed X-ray halo fraction as a function of energy:

$$I(E) = \int_{50''}^{600''} H_f(\theta, E, \Delta E) \times 2\pi\theta d\theta \quad (4)$$

which is also shown for GX 13+1 in Figure 5. Figure 5, which strongly increases at low energies, shows why ROSAT (with a 0.08-2.9 keV bandpass) measured a larger total halo fraction (34%) for GX 13+1 than either of the Einstein (with a 0.1-6 keV bandpass) measurements of 17-18%.

Using the RG approximation, this result be directly compared to the observable dust grain parameters. As discussed in Mauche & Gorenstein (1986), the total scattering due to dust grains is simply $\int da n_{gr}(a)\sigma(a)D$, where $n_{gr}(a)$ is the number density of grains of size

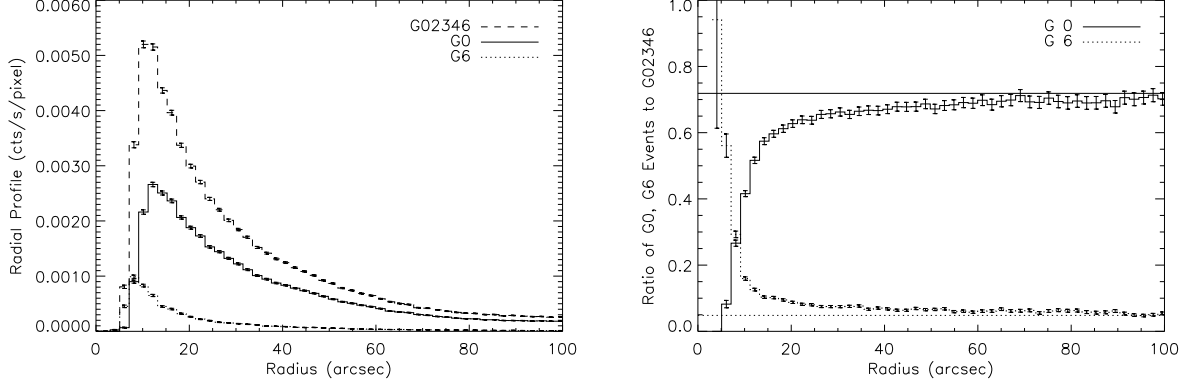


Fig. 3.— (a) The surface brightness of GX 13+1 as a function of radius, including both grade 0, grade 6, and the sum of all “good” grades 0, 2, 3, 4, and 6. Near the source, marginal grade 6 events dominate, while far from the source single-pixel grade 0 events do. (b) The ratio of grade 0 and grade 6 to the sum of all good events, as a function of radius. The horizontal line shows the expected value for grade 0 events far from the source. Within 50'' of the source, pileup is a noticeable issue.

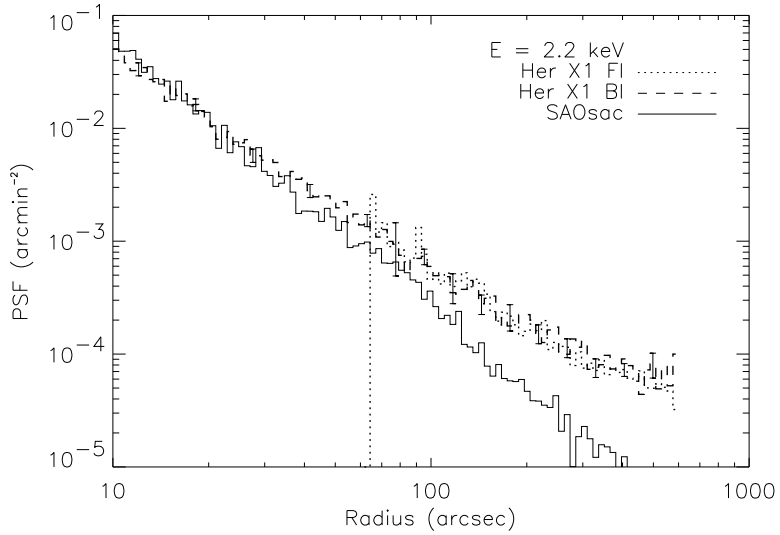


Fig. 4.— The radial profile of Her X-1 in the FI and BI chips between 2.1-2.3 keV, along with the modeled PSF from SAOsac. Her X-1 was on the BI chip S3, so the FI data is available only beyond $\approx 65''$ off-axis. Her X-1 is very lightly absorbed; based on the measured spectrum and assuming a smooth distribution of MRN dust, we calculated that the total X-ray halo will have less than 1.5% of the direct photons.

a , D is the source distance, and $\sigma(a)$ is the total scattering cross section, which can be found by integrating Equation (1) over all angles. The final result is

$$I(E) \approx 0.2 \left(\frac{2Z}{M} \right)^2 \left(\frac{\rho}{3g \text{ cm}^{-3}} \right)^2 \left[\frac{F(E)}{Z} \right]^2 D_{\text{kpc}} E_{\text{keV}}^{-2} \int da n(a) \left(\frac{a}{0.1\mu\text{m}} \right)^4 \left(\frac{n_{gr}(a)}{10^{-12}\text{cm}^{-3}} \right) \quad (5)$$

We can approximate some terms in Equation (5), as $2Z/M \approx 1$ and for $E > 2 \text{ keV}$, $F(E) \approx Z$. With some manipulation, we then get:

$$I(E) = 80.7 \left(\frac{N_{\text{H}}}{10^{22}\text{cm}^{-2}} \right) \left(\frac{\rho}{3g \text{ cm}^{-3}} \right) E_{\text{keV}}^{-2} \int da n(a) \left(\frac{a}{0.1\mu\text{m}} \right) \frac{m_{gr}(a)}{m_H} \quad (6)$$

where $m_{gr}(a)$ is the mass of a grain of radius a . Any dust grain model must include the dust to gas mass ratio (m_{gr}/m_H), the grain density ρ , and the size distribution of the grains $n(a)$. Therefore, given a dust model and a column density N_{H} we can calculate the coefficient term in Equation (6) directly. Since we used the total cross section for scattering, this result is independent of the position of the dust along the line of sight.

We can measure the coefficient term directly from the results we found using Equation (4) by fitting a function with the E^{-2} energy dependence of Equation (5). We found, for GX 13+1,

$$I(E) = H_f E_{\text{keV}}^{-2} = 0.939 \pm 0.028 E_{\text{keV}}^{-2} \quad (7)$$

which is also plotted in Figure 5; the error purely statistical, and does not include any systematic errors. This halo coefficient H_f is an underestimate, since we only include scattering for $50'' < \theta < 600''$. We experimented by changing the upper and lower limits, and found reducing the upper limit by 50% to $400''$ changed H_f only slightly, to 0.89 ± 0.02 . However, increasing the lower limit by 50% to $75''$ led to $H_f = 0.73 \pm 0.02$, a more significant change. We therefore tried reducing the lower limit, although this increases systematic errors due to pileup. A lower limit of $20''$ led to $H_f = 1.28 \pm 0.04$, and a lower limit of $10''$ gave 1.41 ± 0.04 ; within $10''$ of the source the data are visibly affected by pileup. We did a linear extrapolation to the lower limit of $0''$ based on these results and found $H_f = 1.5_{-0.1}^{+0.5}$. These errors are not statistical, but rather are estimated from the variation with the lower limit on the angle. We used a large positive error term because we must assume that the scattered surface brightness within $10''$, which we cannot measure directly, does not increase significantly.

Since the X-ray halo is a function of the size, position, and composition of the dust grains, as well as the source flux and absorption column, to go further in the analysis we must make some assumptions about the dust grains. We first consider the smoothly-distributed dust model, where the dust grain number density is constant along the line of sight. We compare three dust grain models: the MRN model, the Weingartner & Draine (2001; WD) model, and the “extended” MRN model (hereafter the XMRN model) described by Landgraf *et*

al. (2000) and used by Witt, Smith, & Dwek (2001). This model is based on the *in situ* measurements made by *Ulysses* and *Galileo* in the heliosphere, and has the same total mass as the MRN model, but extends the MRN size distribution to $2.0\,\mu\text{m}$, with a break at $0.5\,\mu\text{m}$ from a -3.5 power law to -4.0 for larger grains.

In Figure 6 we show our best-fit results at three energies, using the MRN, WD, and the XMRN dust grain models. The only free parameter in these fits is the total dust grain column, which we allowed to vary independently in each energy band. A number of features are immediately apparent in these results. First, the XMRN model is consistently poor, overestimating the halo at small angles and underestimating it at large angles. At 2.1 keV, this could be partially due to the RG approximation breaking down, but RG should be adequate at 3.7 keV where it is still clearly a poor fit. Although we cannot rule out models such as the XMRN, this dataset certainly does not require them. Secondly, we see that the MRN and WD models both match the halo profile quite well, although the MRN model tends to be the better fit. Including all 10 energies from 2-4 keV, and allowing the column density N_{H} to vary with energy, for the MRN model we found $\chi^2_{\text{red}} = 1.6$, and for the WD model $\chi^2_{\text{red}} = 5.2$ (with 590 degrees of freedom). If we require the column density to be constant, there are 599 degrees of freedom and the best fit for the MRN model is $N_{\text{H}} = 2.22 \pm 0.01 \times 10^{22}\,\text{cm}^{-2}$ with $\chi^2_{\text{red}} = 2.1$. For the WD model, it is $N_{\text{H}} = 1.65 \pm 0.01 \times 10^{22}\,\text{cm}^{-2}$ with $\chi^2_{\text{red}} = 5.8$.

We can check this by comparing the measured halo coefficient of $H_f \approx 1.5$ to the values calculated using Equation (6) and $N_{\text{H}} = 2.9 \times 10^{22}\,\text{cm}^{-2}$. For the MRN, WD, and XMRN models, we calculated halo coefficients of 1.9, 2.8, and 13.1 respectively. As expected, if we use the best-fit N_{H} values for the MRN and WD models, we get much better results: 1.5 and 1.6, respectively. This also shows that the best-fit column density found by fitting the X-ray halo using the MRN model will generally be $\sim 45\%$ larger than fits using the WD model.

The best-fit column density N_{H} shows a slight increase with the X-ray energy for the MRN and WD models, and a significant one for the XMRN model (see Figure 7). The errors shown in Figure 7 are dominated by the errors in the flux measurement. Since we fix each energy band width at 200 eV and do not consider the effect of the varying energy resolution of the ACIS chips, these errors may be somewhat underestimated. It is also possible the quantum efficiency of transfer streak may be lower than expected (M. Bautz, 2002, private communication). If true, this would mean we underestimated the true flux, which would lead us to a larger N_{H} to compensate. For the XMRN model, however, the energy dependence is much steeper over the entire 2-4 keV energy range. The source of the problem could be our use of the RG model, or possibly it is just an artifact caused by the poor overall fit of the XMRN model. We expect to investigate this in a future paper, including applying a

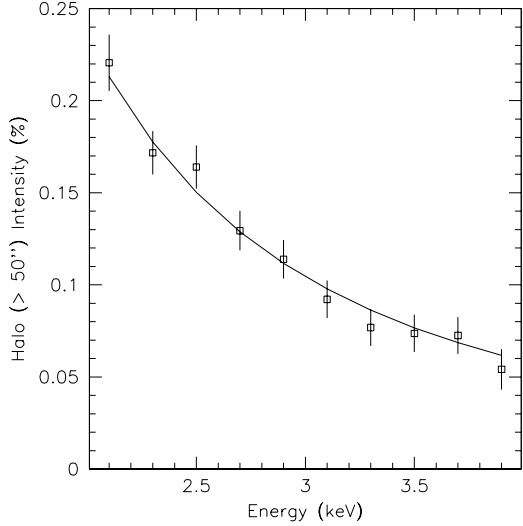


Fig. 5.— The fractional halo intensity (relative to the source flux), as a function of energy along with the best-fit curve $I(E) = 0.939 \pm 0.028 E_{keV}^{-2}$.

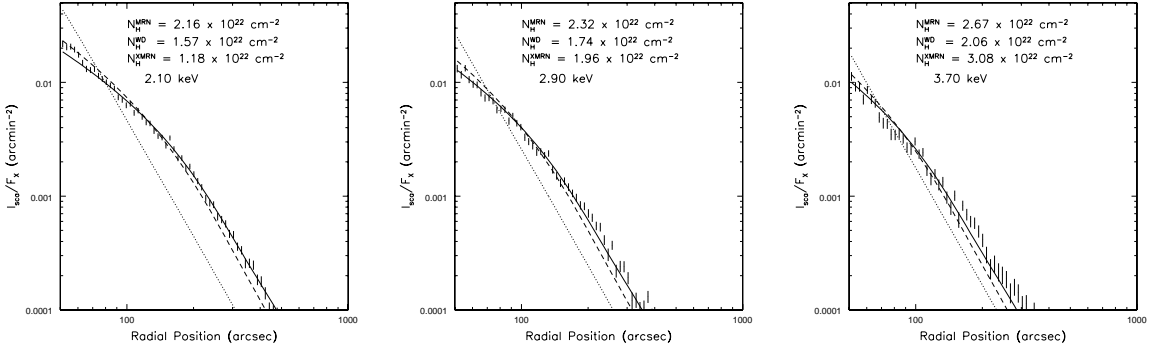


Fig. 6.— X-ray halos observed at 2.1 ± 0.1 , 2.9 ± 0.1 , and 3.7 ± 0.1 keV, fit using smoothly-distributed dust described by the MRN (solid line), WD (dashed line), and the XMRN (dotted line) models. The only free parameter N_H differs substantially between the three grain models; for the XMRN model it appears to systematically increase with X-ray energy.

full Mie solution to the XMRN model.

4.1. Molecular clouds

We have assumed that the dust grains were smoothly distributed along the line of sight (*i.e.* $f(x) \equiv 1$). We can relax this restriction and assume instead that dust grains are found in clumps along the line of sight. This is probably a more realistic model, as the sightline to GX 13+1 crosses two or three spiral arms (Caswell & Haynes 1987; Taylor & Cordes 1993), spaced at about 20%, 40%, and 60% of the distance to GX 13+1. In Figure 8 we show the profiles for E=2.1, 2.9, and 3.7 keV along with fits using MRN dust and four “clouds” placed 20%, 40%, 60%, and 80% of the distance to GX 13+1. The amount of dust in each cloud was allowed to vary independently, but was fixed to be the same value for each X-ray energy. These fits show one result similar to the smoothly-distributed dust case: as the energy increases, the model tends to underpredict the total halo. Since the amount of dust in each cloud was not allowed to vary with energy, the best-fit result ($\chi^2_{red} = 2.0$) slightly exceeds the data at low energies and underestimates at high energies. In addition, the total amount of dust used ($N_H = 2.15 \times 10^{22} \text{ cm}^{-2}$) is similar to the value for the smoothly distributed MRN model.

We also experimented with models using one or two clouds with variable locations and column densities. We could not find an adequate fit with a single cloud model. The lowest $\chi^2_{red} = 5.2$ for the MRN model had a cloud at $x = 0.39$ and column density $N_H = 1.65 \times 10^{22} \text{ cm}^{-2}$. Fitting two clouds with variable positions and column densities, however, we found a minimum $\chi^2_{red} = 2.31$, nearly as good a fit as Galactic arm model with four fixed clouds. The best-fit cloud parameters are $N_H = 1.15 \pm 0.01 \times 10^{22} \text{ cm}^{-2}$ at $x = 0.204 \pm 0.007$ and $N_H = 1.19_{-0.45}^{+0.02} \times 10^{22} \text{ cm}^{-2}$ at $x = 0.80 \pm 0.08$.

These fits show that two or three “dust clouds” can fit the data nearly as well as the smoothly-distributed case. One cloud must be near GX 13+1 to reproduce the scattering seen at $\theta < 100''$ and the second cloud must be near the observer to cause the more extended scattering. In the four fixed cloud model, the clouds 40% and 60% of the distance to GX 13+1 have the smallest column densities; in the two cloud model, the data tend to the 20% and 80% positions naturally. This suggests that the nearest spiral arm contains substantial dust, along with material near the Galactic center.

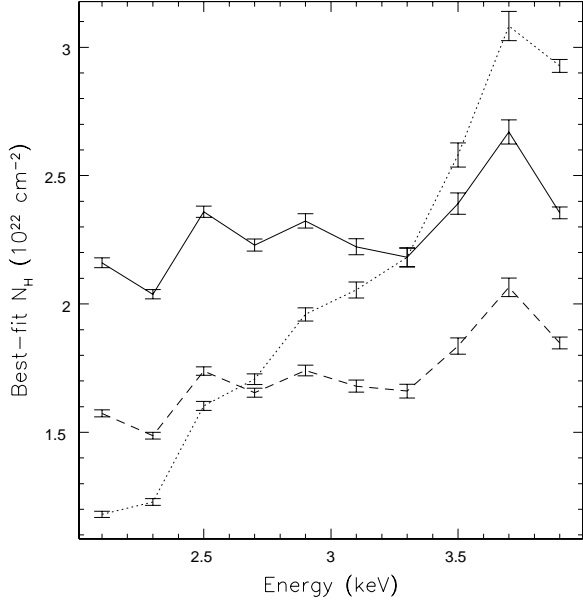


Fig. 7.— The best-fit N_{H} as a function of X-ray energy both for the MRN model (solid line), the WD model (dashed line), and the XMRN model (dotted line). The slight increase with energy, especially above 3.3 keV, is clear in all cases although it is far worse in the XMRN case. The error bars are statistical. The systematic error is dominated by the flux measurement, and there may be calibration problems with the higher energies.

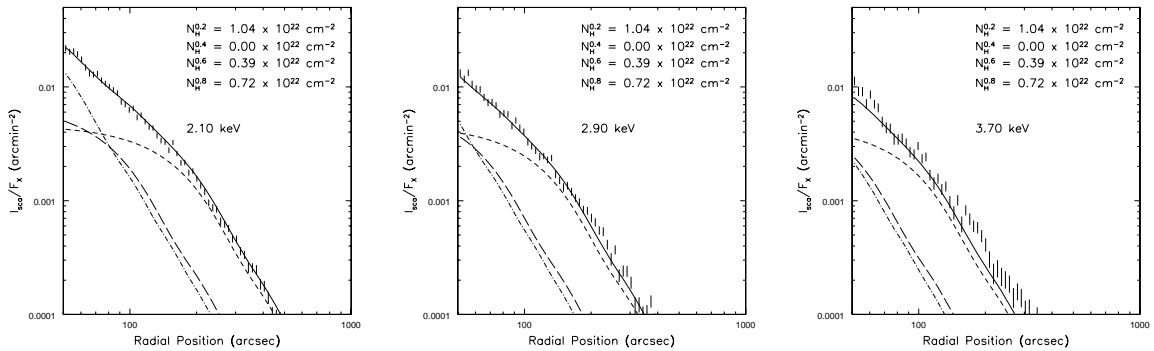


Fig. 8.— X-ray halos observed at 2.1 ± 0.1 , 2.9 ± 0.1 , and 3.7 ± 0.1 keV, fit using four evenly-spaced clouds of dust (using an MRN model) at 20%, 40%, 60%, and 80% of the distance to GX 13+1. Each dust cloud has a variable amount of dust parameterized by N_{H} . The best-fit total scattering is given by the solid line. The scattering from the cloud at 20% is shown by the dashed line, at 60% by the long-dashed line, and at 80% by the dot-dashed line.

5. Conclusions

The high angular resolution of the *Chandra* telescope provides the best data to date of any X-ray halo, while the energy range and resolution allow us to explore the halo’s behavior as a function of energy with moderate resolution. Although we limited our investigation to off-axis angles greater than $50''$ to avoid any possible contamination by pileup, our models tended to fit reasonably well for smaller angles and we may be able to relax this in the future. We also limited our analysis to energies higher than 2 keV, to allow the use of the RG model and to avoid the difficulties involved in including multiple X-ray scattering. These issues can be addressed with improved modeling techniques, which we plan to include in a future paper.

We were able to measure, for the first time, the halo coefficient $H_f = 1.5^{+0.5}_{-0.1}$ by fitting the total halo intensity (relative to the source intensity) as a function of energy to the equation $I(E) = H_f E_{\text{keV}}^{-2}$. Physically, H_f is the halo fraction at 1 keV, but using the RG approximation it can be compared directly to dust model parameters via a simple calculation (see Eq. (6)). The large errors in our measurement are due largely to pileup; more X-ray halo measurements are clearly needed to get more halo coefficients. We expect this will soon provide a tight constraint for dust models for the ISM.

We have found that models with low density “fluffy” dust are not supported by these data. The X-ray halo surface brightness is proportional to $N_{\text{H}} \times \rho_{\text{dust}}^2$. For the MRN and WD models, we found $N_{\text{H}} = 2.22 \pm 0.01 \times 10^{22} \text{ cm}^{-2}$ and $1.65 \pm 0.01 \times 10^{22} \text{ cm}^{-2}$, respectively. The true column density to GX 13+1 is difficult to measure, but we infer from infrared observations that $N_{\text{H}} \lesssim 2.7 \times 10^{22} \text{ cm}^{-2}$ and from the ASCA data that $N_{\text{H}} = 2.9 \pm 0.1 \times 10^{22} \text{ cm}^{-2}$. So at most, the true column density to GX 13+1 is only twice the lowest value determined from the halo observations, which allows for a dust grain density at most 30% lower than the nominal value, and likely less. A “fluffy” dust model may exist that matches the observations, but it would have to include substantially more dust grains to maintain the total scattering cross section. For example, an MRN-type model with $\rho = \rho_{\text{MRN}}/5$ would need 25 times more dust grains to achieve the same total scattering.

At the same time, the large dust grain model used in Witt, Smith & Dwek (2001) is also not supported by these data, in agreement with the results of Predehl & Schmitt (1995). The large dust grains cause the scattering at very small observed angles ($< 100''$) to increase dramatically. The ROSAT PSPC data used by Witt, Smith & Dwek (2001) had only one point at $100''$, which drove the fit to prefer the large dust grain model. *Chandra*’s superior angular and energy resolution (and range) show that for this line of sight at least, large dust grains are not significant. Finally, we also found that the data are better fit by the MRN model than the WD model, although enough potential calibration issues remain to keep this

an open issue.

We would like to thank Terry Gaetz for obtaining the Her X-1 calibration observations, Diab Jerius for helping us with SAOsac, and the entire CXC calibration team for their substantial contribution to this project. We also thank Eli Dwek for many helpful discussions, and the referee Peter Predehl for his comments and suggestions which greatly improved this paper. This work was supported by the Chandra X-ray Science Center (NASA contract NAS8-39073) and NASA Chandra observation grant GO0-1107X.

REFERENCES

Bandyopadhyay, R. M., Shahbaz, T., Charles, P. A. & Naylor, T. 1999, MNRAS, 306, 417
Berendsen, S. G. H., Fender, R., Kuulkers, E., Heise, J. & van der Klis, M. 2000, MNRAS, 318, 599
Caswell, J. L. & Haynes, R. F. 1987, A&A, 171, 261
Catura, R. C. 1983, ApJ, 275, 645
Christian, D. J. & Swank, J. H. 1997, ApJS, 109, 177
Dickey, J. M & Lockman, F. J. 1990, ARA&A, 28, 215
Draine, B. T. & Lee, H. M. 1984, ApJ, 285, 89
Garcia, M. R., Grindlay, J. E., Bailyn, C. D., Pipher, J. L., Shure, M. A., & Woodward, C. E. 1992, AJ, 103, 1325
Hasinger, G. & van der Klis, M. 1989, A&A, 225, 79.
Henke, B. L. 1981, in “Low Energy X-Ray Diagnostics”, ed. D. T. Attwood and B. L. Henke (New York, AIP)
Homan, J., van der Klis, M., Wijnands, R., Vaughan, B. & Kuulkers, E. 1998, ApJL, 499, L41
Landgraf, M., Baggaley, W. J., Grün, E., Kröger, H., & Linkert, G. 2000 J. Geophys. Res., 105, 10343
Liu, Q. Z., van Paradijs, J., & van den Heuvel, E. P. J. 2001, A&A, 368, 1021
Mathis, J. S. & Lee, C. W. 1991, ApJ, 376, 490
Mathis, J. S., Cohen, D., Finley, J. P., & Krautter, J. 1995, ApJ, 449, 320
Mathis, J. S., Rumpl, W. & Nordsieck, K. H. 1977, ApJ, 217, 425 (MRN)
Mauche, C. W. & Gorenstein, P. 1986, ApJ, 302, 371

Mitsuda *et al.* 1984, PASJ, 36, 741
Makishima *et al.* 1986, ApJ308, 635
Overbeck, J. W. 1965, ApJ, 141, 864
Predehl, P. & Schmitt, J. H. H. M. 1995, A&A, 246, L40
Schulz, N. S., Hasinger, G., & Trümper, J. 1989, A&A, 225, 48
Seward, F. D. 2000, in Allen’s Astrophysical Quantities, ed. A. N. Cox. (New York: AIP), 183
Smith, R. K. & Dwek, E. 1998, ApJ, 503, 831
Taylor, J. H. & Cordes, J. M. 1993, ApJ, 411, 674
Ueda, Y., Asai, K., Yamaoka, K., Dotani, T., & Inoue, H. 2001, ApJ, 556, L87
Weingartner, J. C. & Draine, B. T. 2001, ApJ, 548, 296 (WD)
Witt, A., Smith, R. K. & Dwek, E. 2001, ApJ, 550, 201